

1 **Practical considerations for computing dimensional spectra from gridded**  
2 **data**

3 Dale Durran\*, Jonathan A. Weyn, Maximo Q. Menchaca

4 *Department of Atmospheric Sciences, University of Washington*

5 Revised July 6, 2017

6 *\*Corresponding author address:* Dept. of Atmospheric Sciences, University of Washington, Box  
7 351640, Seattle, WA 98195.

8 E-mail: drdee@uw.edu

## ABSTRACT

9 Spectra are often computed from gridded data to determine the horizontal-  
10 scale dependence of quantities such as kinetic energy, vertical velocity or  
11 perturbation potential temperature. This paper discusses several important  
12 considerations for the practical computation of such spectra. To ensure that  
13 the sum of the spectral energy densities in wavenumber space matches the  
14 sum of the energies in the physical domain (the discrete Parseval relation),  
15 the constant coefficient multiplying the spectral energy density must properly  
16 account for the way the discrete Fourier transform pair is normalized. The  
17 normalization factor appropriate of many older FORTRAN based fast Fourier  
18 transforms (FFTs) differs from that in Matlab and Python's `numpy.fft`, and as  
19 a consequence, the correct scaling factor for the kinetic energy (KE) spectral  
20 density differs between one-dimensional FFTs computed using these two ap-  
21 proaches by a factor equal to the square of the number of physical grid points.  
22 A common algorithm used to compute two-dimensional spectra as a function  
23 of the total-wavenumber magnitude sums the contributions from all pairs of  
24  $x$ - and  $y$ -component wavenumbers whose vector magnitude lies with a series  
25 of bins. This approach introduces systematic short-wavelength noise, which  
26 can be largely eliminated though a simple multiplicative correction. One- and  
27 two-dimensional spectra will differ by a constant if computed for flows in  
28 which the KE spectral density decreases as a function of the wavenumber to  
29 some negative power. This constant is evaluated and the extension of theoret-  
30 ical results to numerically computed FFTs is examined.

## 31 1. Introduction

32 When computing spectra from observed or model data, the main focus is often on the slope of  
33 the spectrum as a function of wavenumber on a log-log plot. Nevertheless, if such spectra are to  
34 be quantitatively compared with those obtained in other studies (as in, for example, Skamarock  
35 2004; Hamilton et al. 2008), it is important to be able to correctly compute the magnitude of the  
36 energy spectral density. The goal of this article is to facilitate such comparisons.

37 The discrete Fourier transform (DFT) of a vector  $\mathbf{u}$  of length  $N$  is often defined as

$$\hat{u}_m = n_1 \sum_{j=1}^N u_j \omega_N^{(m-1)(j-1)}, \quad (1)$$

38 together with the inverse transform

$$u_j = n_2 \sum_{m=1}^N \hat{u}_m \omega_N^{-(m-1)(j-1)}, \quad (2)$$

39 where  $n_1 n_2 = 1/N$  and, following the typical “roots of unity” notation,  $\omega_N = e^{-2\pi i/N}$  (Durrant  
40 2010). Neither the choice of the signs in the exponents nor the distribution of the normalization  
41 factors  $n_1$  and  $n_2$  between (1) and (2) are standardized. The only requirement is that the product of  
42 the normalization factors equals  $1/N$  and that the exponents have opposite signs. Many classical  
43 treatments of the DFT follow the convention  $(n_1, n_2) = (1/N, 1)$  (Cooley et al. 1970; Durrant 2010),  
44 but the DFT in Matlab and Python (specifically Matlab’s FFT–IFFT pair and the default option in  
45 Python’s `numpy.fft` module) follow the opposite convention  $(n_1, n_2) = (1, 1/N)$ . The choice of  
46  $(n_1, n_2)$  impacts the discrete Parseval relation and as a consequence, the dimensional coefficients  
47 that should appear in the computation of energy spectral densities. One purpose of this article is to  
48 clarify the factors that should appear in dimensional atmospheric spectra, for example to compare  
49 commonly computed horizontal kinetic energy (KE) spectra in gridded models with observations  
50 (Nastrom and Gage 1985; Cho et al. 1999). The correct dimensional scaling for one-dimensional  
51 spectra is discussed in Section 2, while that for two-dimensional spectra is presented in Section 3.

52 The second purpose of this article is to highlight a simple technique for reducing systematic  
53 noise in the computation of two-dimensional spectra. Two-dimensional spectra are typically eval-  
54 uated as a function of total wavenumber  $k_h = (k_x^2 + k_y^2)^{1/2}$ , where  $k_x$  and  $k_y$  are the wavenumbers  
55 parallel to each coordinate axis, which we label as  $x$  and  $y$ . For continuous Fourier transforms,  
56 the KE spectral density at  $k_h$  is evaluated by integrating around a ring of radius  $k_h$  centered at the  
57 origin in the  $k_x$ - $k_y$  plane. The corresponding calculation for discrete data often follows the proce-  
58 dure detailed in Errico (1985) in which the integral around a ring in the  $k_x$ - $k_y$  plane is replaced by  
59 summing up the energies of all  $(k_x, k_y)$  pairs that lie with annular rings. This procedure introduces  
60 *systematic* noise, and as briefly noted in Tanguay et al. (1995), such noise can be easily eliminated  
61 through multiplication by a compensating factor, as will be discussed in Section 4.

62 The final topic, investigated in Section 5, is the difference in the magnitude of one-dimensional  
63 and two-dimensional KE spectra computed for the same flow. The theoretical discussion in Leith  
64 (1971) for isotropic horizontally non-divergent flow is first generalized; then we examine the influ-  
65 ence of the numerical approximations that accompany the computation of discrete Fourier trans-  
66 forms. Finally we compare one-dimensional and two-dimensional KE spectra in a physically  
67 relevant divergent, anisotropic flow.

68 Throughout the following we assume the data are periodic. If the data are not periodic, they can  
69 be made periodic by removing the linear trend along lines parallel to each coordinate axis (Errico  
70 1985), or fitting a two-dimensional plane to the data and then multiplying the values near the  
71 edges by a function that smoothly approaches zero at the boundary (Salvador et al. 1999). Denis  
72 et al. (2002) suggest the discrete cosine transform (DCT) offers the best approach for computing  
73 the spectra of aperiodic fields. We do not discuss the DCT here, but all of our formulas may be  
74 applied, with appropriate modification, to the DCT. Indeed, the application of the cosine transform  
75 to aperiodic data is conceptually equivalent to imposing symmetry boundary conditions at both

76 edges of the domain, mirroring the existing data across one symmetry boundary, and applying a  
 77 conventional Fourier transform on the expanded domain.

## 78 **2. One-dimensional KE spectra**

79 We begin by considering the properties of continuous fields. Neglecting the fluid density,  
 80 the time- and space-averaged KE equals the KE spectral density  $E(k)$  integrated over positive  
 81 wavenumbers

$$\left( \frac{\overline{\mathbf{u} \cdot \mathbf{u}}}{2} \right) = \int_0^{\infty} E(k) dk, \quad (3)$$

82 where  $\mathbf{u} = (u, v)$  is the horizontal velocity vector and the spatial average is denoted by an overbar  
 83 (Tennekes and Lumley 1972, (8.1.5)). The calculations for time averaging are obvious and will be  
 84 ignored throughout the following.

85 Defining the continuous Fourier transform and its inverse as

$$\hat{u}(k) = \int_{-\infty}^{\infty} u(x) e^{2\pi i x k} dx,$$

$$u(x) = \int_{-\infty}^{\infty} \hat{u}(k) e^{-2\pi i x k} dk,$$

87 The Parseval theorem for continuous functions may be expressed as

$$\overline{(u^2)} = \int_{-\infty}^{\infty} \hat{u}(k) \hat{u}^*(k) dk.$$

88 Since  $u$  is real,  $\hat{u}(k) = \hat{u}^*(-k)$ , and thus

$$\frac{1}{2} \int_{-\infty}^{\infty} \hat{u}(k) \hat{u}^*(k) dk = \int_0^{\infty} \hat{u}(k) \hat{u}^*(k) dk,$$

89 from which it follows that the KE spectral density in (3) may be written

$$E(k) = \hat{u}(k) \hat{u}^*(k) + \hat{v}(k) \hat{v}^*(k).$$

90 Our next goal is to find expressions for  $E(k)$  appropriate for discrete versions of (3). Let  $(u_j, v_j)$   
 91 be the set of  $N$  gridpoint values of the  $x$ - and  $y$ -component velocities on a periodic mesh such that

$$x_j = (j - 1)\Delta x, \quad j = 1, 2, \dots, N, \quad (4)$$

92 where  $\Delta x$  is the grid spacing and values at  $x = 0$  match those at  $x = N\Delta x \equiv L$ . FFTs are most  
 93 efficient when  $N$  is a power of two, or the product of powers of small prime numbers. We will  
 94 therefore assume that  $N$  is even, in which case the shortest wavelength on the mesh is exactly  
 95  $2\Delta x$ ; the largest wavenumber is exactly  $k_{\max} = \pi/\Delta x$ , and the Fourier modes corresponding to  
 96 wavenumbers  $k_{\max}$  and  $-k_{\max}$  are linearly dependent *on the discrete mesh*. As a consequence of  
 97 this linear dependence, when  $N$  is even, the vector of Fourier coefficients  $\hat{u}$  contains pairs of entries  
 98 for positive and negative wavenumbers for every wavelength except those corresponding to  $k = 0$   
 99 and  $k_{\max}$ . In our subsequent notation, we will assume that the coefficients of  $k = 0$  and  $k = k_{\max}$   
 100 are indexed in (2) when  $m = 1$  and  $m = N/2 + 1 \equiv N_m$ , respectively.

101 Many Fortran routines for computing fast Fourier transforms, including FFTW and those in fft-  
 102 pack, are unnormalized and require the user to explicitly specify  $n_1$  and  $n_2$ , in which case the  
 103 simplest discrete expressions for  $E(k)$  are obtained using  $(n_1, n_2) = (1/N, 1)$ . Since the case  
 104  $(n_1, n_2) = (1/N, 1)$  is simplest, we consider it first; this is the opposite convention from that in  
 105 Matlab and Python's `numpy.fft`.

106 *a. Case  $n_1 = 1/N$*

107 If the  $1/N$  normalization factor is attached to the forward transform ( $n_1 = 1/N$ ), as derived in  
 108 the Appendix, the discrete Parseval relation becomes

$$\frac{1}{N} \sum_{j=1}^N u_j^2 = \sum_{m=1}^N \hat{u}_m \hat{u}_m^*, \quad (5)$$

109 implying that

$$\frac{1}{L} \sum_{j=1}^N \frac{u_j^2 + v_j^2}{2} \Delta x = \frac{1}{2} \sum_{m=1}^N (\hat{u}_m \hat{u}_m^* + \hat{v}_m \hat{v}_m^*) = \frac{1}{2\Delta k} \sum_{m=1}^N (\hat{u}_m \hat{u}_m^* + \hat{v}_m \hat{v}_m^*) \Delta k. \quad (6)$$

110 To identify an appropriate expression for  $\Delta k$ , note that the sum on the RHS of (6) represents a  
 111 numerical quadrature such that

$$\sum_{m=1}^N (\hat{u}_m \hat{u}_m^* + \hat{v}_m \hat{v}_m^*) \Delta k \approx \int_{-k_{\max}}^{k_{\max}} \hat{u}(k) \hat{u}^*(k) + \hat{v}(k) \hat{v}^*(k) dk \quad (7)$$

112 Temporarily assume  $\hat{u}(k) \hat{u}^*(k) + \hat{v}(k) \hat{v}^*(k)$  and  $\hat{u}_m \hat{u}_m^* + \hat{v}_m \hat{v}_m^*$  are one for all  $k$ , then  $N\Delta k = 2k_{\max} =$   
 113  $2\pi/\Delta x$ , and thus,  $\Delta k = 2\pi/(N\Delta x) = 2\pi/L$ . This is a natural choice in which  $\Delta k$  is simply the  
 114 smallest nonzero value of  $k$  in the periodic domain.

115 Replacing the summation with twice the sum over positive wavenumbers (except for  $k_{\max}$ ), and  
 116 skipping wavenumber zero because we can assume the mean was removed before the spectral  
 117 analysis, the discrete relation (6) may be expressed in a form directly comparable to (3) as

$$\frac{1}{L} \sum_{j=1}^N \frac{u_j^2 + v_j^2}{2} \Delta x = \sum_{m=2}^{N_m} \tilde{E}_m \Delta k, \quad (8)$$

118 where the discrete KE spectral density is

$$\tilde{E}_m = \frac{1}{(1 + \delta_{m,N_m})} \frac{\hat{u}_m \hat{u}_m^* + \hat{v}_m \hat{v}_m^*}{\Delta k} = \frac{L}{2\pi(1 + \delta_{m,N_m})} (\hat{u}_m \hat{u}_m^* + \hat{v}_m \hat{v}_m^*), \quad (9)$$

119 and  $\delta_{m,N_m}$  is the Kronecker delta; (the factor including this term prevents the spectral power from  
 120 being erroneously doubled at  $k = k_{\max}$ ).

121 *b. Case  $n_2 = 1/N$*

122 Now suppose that following Matlab and Python's `numpy.fft`, the  $1/N$  normalization factor is  
 123 attached to the inverse transform ( $n_2 = 1/N$ ). Then the discrete Parseval relation becomes

$$\sum_{j=1}^N u_j^2 = \frac{1}{N} \sum_{m=1}^N \hat{u}_m \hat{u}_m^*, \quad (10)$$

124 and the average KE in a domain of length  $L$  satisfies

$$\frac{1}{L} \sum_{j=1}^N \frac{u_j^2 + v_j^2}{2} \Delta x = \frac{\Delta x}{2NL} \sum_{m=1}^N (\hat{u}_m \hat{u}_m^* + \hat{v}_m \hat{v}_m^*) \quad (11)$$

125 The left side of (11) clearly approximates the left side of (3). The right side of (11) is again a sum  
 126 over both positive and negative wavenumbers, which assuming zero amplitude at wavenumber  
 127 zero, can be replaced by twice the sum over positive wavenumbers (except  $k_{\max}$ ). Recalling that  
 128  $\Delta k = 2\pi/L$ , (11) may therefore be expressed as

$$\frac{1}{L} \sum_{j=1}^N \frac{u_j^2 + v_j^2}{2} \Delta x = \sum_{m=2}^{N_m} \check{E}_m \Delta k, \quad (12)$$

129 where the discrete KE spectral density  $\check{E}_m$  for this alternative normalization is<sup>1</sup>

$$\check{E}_m = \frac{\Delta x}{2\pi N(1 + \delta_{m, N_m})} (\hat{u}_m \hat{u}_m^* + \hat{v}_m \hat{v}_m^*). \quad (13)$$

130 Noting that

$$\check{E}_m = \tilde{E}_m / N^2,$$

131 we conclude that the different choices for normalizing the discrete Fourier transform introduce  
 132 large differences in the scaling of the KE spectral density.

### 133 3. Two-dimensional KE spectra

134 Let  $k_x$  and  $k_y$  be the dimensional wavenumbers in the  $x$  and  $y$  directions, and  $\hat{u}(k_x, k_y)$  and  
 135  $\hat{v}(k_x, k_y)$  be the two-dimensional Fourier transforms of the velocity field. Defining the total hori-  
 136 zontal wavenumber as  $k_h = (k_x^2 + k_y^2)^{1/2}$ , the integral of the two-dimensional KE spectral density  
 137  $E(k_h)$  again equals the integral of the KE over the physical domain:

$$\left( \frac{\overline{\mathbf{u} \cdot \mathbf{u}}}{2} \right) = \int_0^\infty E(k_h) dk_h, \quad (14)$$

---

<sup>1</sup>The one-dimensional spectra computed in Durran and Weyn (2016) erroneously omitted a factor of  $1/\pi$ , which would have brought those results into closer agreement with observations.



138 where  $E(k_h)$  is the integral over all pairs  $(k_x, k_y)$  such that  $k_h = (k_x^2 + k_y^2)^{1/2}$ . To be specific, let  
 139  $\mathbf{c}(\theta) = (k_h \cos \theta, k_h \sin \theta)$ , then

$$E(k_h) = \frac{1}{2} \int_0^{2\pi} [\hat{u}(\mathbf{c}(\theta))\hat{u}^*(\mathbf{c}(\theta)) + \hat{v}(\mathbf{c}(\theta))\hat{v}^*(\mathbf{c}(\theta))] k_h d\theta. \quad (15)$$

140 We wish to determine the discrete approximations to  $E(k_h)$  appropriate for horizontal velocities  
 141  $(u_{r,s}, v_{r,s})$  defined at gridpoints on a periodic mesh

$$x_r = (r-1)\Delta x, \quad j = 1, 2, \dots, N_x; \quad y_s = (s-1)\Delta y, \quad s = 1, 2, \dots, N_y.$$

142 *a. Case  $n_1 = 1/N$*

143 The appropriate discrete Parseval relation (5) generalizes to two-dimensions in a straight forward  
 144 way, such that

$$\frac{1}{N_x N_y} \sum_{r=1}^{N_x} \sum_{s=1}^{N_y} u_{r,s}^2 + v_{r,s}^2 = \sum_{l=1}^{N_x} \sum_{m=1}^{N_y} \hat{u}_{l,m} \hat{u}_{l,m}^* + \hat{v}_{l,m} \hat{v}_{l,m}^*. \quad (16)$$

145 Denoting the extent of the  $x$  and  $y$  domains as  $L_x = N_x \Delta x$  and  $L_y = N_y \Delta y$ , and applying the same  
 146 reasoning as in the 1D case, we obtain  $\Delta k_x = 2\pi/L_x$  and  $\Delta k_y = 2\pi/L_y$ , allowing (16) to be written

$$\frac{1}{L_x L_y} \sum_{r=1}^{N_x} \sum_{s=1}^{N_y} \frac{u_{r,s}^2 + v_{r,s}^2}{2} \Delta x \Delta y = \frac{L_x L_y}{8\pi^2} \sum_{l=1}^{N_x} \sum_{m=1}^{N_y} (\hat{u}_{l,m} \hat{u}_{l,m}^* + \hat{v}_{l,m} \hat{v}_{l,m}^*) \Delta k_x \Delta k_y. \quad (17)$$

147 The left side of (17) approximates the left side of (3), but the right side needs to be replaced by a  
 148 sum over the total wavenumber.

149 We discretize the 2D wavenumber in multiples of the maximum one-dimensional wavenumber,  
 150  $\Delta k_h = \max(\Delta k_x, \Delta k_y)$ , such that

$$k_p = p\Delta k_h, \quad p = 1, 2, \dots, N_{\max},$$

151 where  $N_{\max} = \lceil \sqrt{2} \max(N_x/2, N_y/2) \rceil$ . Defining  $R(p)$  as the set of wavenumber indices  $(l, m)$   
 152 satisfying

$$k_p - \Delta k_h/2 \leq (k_{x_l}^2 + k_{y_m}^2)^{1/2} < k_p + \Delta k_h/2, \quad (18)$$

153 (17) may be written

$$\frac{1}{L_x L_y} \sum_{r=1}^{N_x} \sum_{s=1}^{N_y} \frac{u_{r,s}^2 + v_{r,s}^2}{2} \Delta x \Delta y = \sum_{p=1}^{N_{\max}} \tilde{E}(k_p) \Delta k_h, \quad (19)$$

154 where

$$\tilde{E}(k_p) = \frac{L_x L_y \min(\Delta k_x, \Delta k_y)}{8\pi^2} \sum_{l,m \in R(p)} (\hat{u}_{l,m} \hat{u}_{l,m}^* + \hat{v}_{l,m} \hat{v}_{l,m}^*). \quad (20)$$

155 This summation over total wavenumber is similar to that in Errico (1985), except that instead of  
 156 choosing  $\Delta k_h$  to be  $\min(\Delta k_x, \Delta k_y)$ , we set it equal to the maximum to reduce the noise that would  
 157 arise using the narrower spectral band.

158 For an isotropic grid with  $\Delta x = \Delta y$  and  $L_x = L_y \equiv L$ ,  $\Delta k_x = \Delta k_y = \Delta k_h$ ,

$$\tilde{E}(k_p) = \frac{L}{4\pi} \sum_{l,m \in R(p)} (\hat{u}_{l,m} \hat{u}_{l,m}^* + \hat{v}_{l,m} \hat{v}_{l,m}^*). \quad (21)$$

159 We would only plot the spectrum  $\tilde{E}(k_p)$  through wavenumber  $k_h = N\Delta k_h/2$  because the data for  
 160 higher wavenumbers are incomplete on the discrete mesh.

161 *b. Case  $n_2 = 1/N$*

162 The Parseval relation becomes

$$\sum_{r=1}^{N_x} \sum_{s=1}^{N_y} u_{r,s}^2 + v_{r,s}^2 = \frac{1}{N_x N_y} \sum_{l=1}^{N_x} \sum_{m=1}^{N_y} \hat{u}_{l,m} \hat{u}_{l,m}^* + \hat{v}_{l,m} \hat{v}_{l,m}^*,$$

163 Using the notation introduced in the preceding subsection, the average KE in the domain satisfies

$$\begin{aligned} \frac{1}{L_x L_y} \sum_{r=1}^{N_x} \sum_{s=1}^{N_y} \frac{u_{r,s}^2 + v_{r,s}^2}{2} \Delta x \Delta y &= \frac{\Delta x \Delta y}{2N_x N_y L_x L_y} \sum_{l=1}^{N_x} \sum_{m=1}^{N_y} \hat{u}_{l,m} \hat{u}_{l,m}^* + \hat{v}_{l,m} \hat{v}_{l,m}^* \\ &= \frac{\Delta x \Delta y}{8\pi^2 N_x N_y} \sum_{l=1}^{N_x} \sum_{m=1}^{N_y} (\hat{u}_{l,m} \hat{u}_{l,m}^* + \hat{v}_{l,m} \hat{v}_{l,m}^*) \Delta k_x \Delta k_y \end{aligned} \quad (22)$$

164 Summing over annular rings in the  $k_x$ - $k_y$  plane, one obtains

$$\frac{1}{L_x L_y} \sum_{r=1}^{N_x} \sum_{s=1}^{N_y} \frac{u_{r,s}^2 + v_{r,s}^2}{2} \Delta x \Delta y = \sum_{p=1}^{N_{\max}} \tilde{E}(k_p) \Delta k_h, \quad (23)$$

165 where

$$\check{E}(k_p) = \frac{\Delta x \Delta y \min(\Delta k_x, \Delta k_y)}{8\pi^2 N_x N_y} \sum_{l,m \in R(p)} (\hat{u}_{l,m} \hat{u}_{l,m}^* + \hat{v}_{l,m} \hat{v}_{l,m}^*). \quad (24)$$

166 For an isotropic square grid,

$$\check{E}(k_p) = \frac{L}{4\pi N^4} \sum_{l,m \in R(p)} (\hat{u}_{l,m} \hat{u}_{l,m}^* + \hat{v}_{l,m} \hat{v}_{l,m}^*), \quad (25)$$

167 implying that in the case of two-dimensional spectra,

$$\check{E}(k_p) = \tilde{E}(k_p)/N^4.$$

#### 168 4. Reducing discretization noise in 2D spectra

169 The summation over annular rings in the  $k_x$ - $k_y$  plane computed, for example in (20), introduces  
 170 *systematic* noise in 2D spectra because the number (or count  $C(p)$ ) of wavenumber pairs in set  
 171  $R(p)$  does not increase smoothly with  $k_p$ . As noted in Tanguay et al. (1995), one can compensate  
 172 for this systematic noise by multiplying the KE spectral density at each discrete  $k_p$  by

$$\frac{2\pi k_p}{\Delta k_{\perp}} \cdot \frac{1}{C(p)}, \quad (26)$$

173 where  $\Delta k_{\perp} = \min(\Delta k_x, \Delta k_y)$ . Given that  $\Delta k_h = \max(\Delta k_x, \Delta k_y)$  is the discrete grid interval along the  
 174 radial direction,  $\Delta k_{\perp}$  may be interpreted as the effective grid interval around the circumference of  
 175 the annulus (18) in the  $k_x$ - $k_y$  plane. Thus, (26) represents the ratio of the number of wavenumber  
 176 pairs that would be expected around a ring of radius  $k_p$  divided by the actual number of pairs  
 177 falling in the annulus (18).

178 A few previous studies also mention the use of factors similar to (26) to reduce noise (Bartello  
 179 1995; Waite 2016), but it is unclear how commonly this type of compensation has been employed.  
 180 In particular, it is not discussed in Errico (1985), which gives a detailed algorithm for the computa-  
 181 tion of two-dimensional spectra that has been frequently cited. In the remainder of this section, we

182 document the significant improvements that can be achieved using such compensation and suggest  
 183 a modest improvement to the formulation in (26). Note that the discrete Parseval relation no longer  
 184 holds if the spectral density is multiplied by (26) or the similar factor (28).

185 In an isotropic square domain,  $\Delta k_{\perp} = 2\pi/L$  and the factor in (26) may be alternatively expressed  
 186  $Lk_p/C(p)$ . Fig. 1 shows  $Lk_p = Nk_p\Delta x$  plotted as a function of  $k_p\Delta x$  as the black dashed line  
 187 terminating at the value of  $k_p\Delta x$  corresponding to a  $2\Delta x$  wave. Also shown in Fig. 1 is  $C(p)/N$   
 188 for the case  $N = 128$ , which roughly follows the line  $Nk_p\Delta x$  over the interval  $[0, \pi]$  and then  
 189 quickly falls to one at  $k_p\Delta x = \sqrt{2}\pi$  because of the rapid increase in the number of missing  $(k_x, k_y)$   
 190 pairs at wavelengths shorter than  $2\Delta x$ . The fluctuations of  $C(p)/N$  about the line  $Nk_p\Delta x$  are not  
 191 random; they leave an imprint on two-dimensional spectra that are computed using the summation  
 192 procedure in (20), and they can be removed through multiplication by the factor (26).

193 The distribution of the data from two-dimensional FFTs is very nonlinear in spectral space, with  
 194 just a few widely spaced points corresponding to the smallest wavenumbers, and many closely  
 195 spaced points at larger wavenumbers. To improve the performance of the preceding noise com-  
 196 pensation at very small wavenumbers, where the numerical resolution as a function of  $k_h$  is very  
 197 coarse, it is helpful to replace  $k_p$  in (26) by the average  $k_h$  for all wavenumber pairs in  $R(p)$ , which  
 198 will be denoted by  $\bar{k}_p$ . Then the noise-compensated spectral density corresponding to (20) would  
 199 become

$$\tilde{E}_c(k_p) = \frac{L_x L_y \bar{k}_p}{4\pi C(p)} \sum_{l,m \in R(p)} (\hat{u}_{l,m} \hat{u}_{l,m}^* + \hat{v}_{l,m} \hat{v}_{l,m}^*). \quad (27)$$

200 The effectiveness of this noise removal procedure is illustrated in two examples. First consider  
 201 a randomly distributed scalar variable with zero mean defined on a  $128 \times 128$  grid-point square  
 202 domain. The energy spectral density  $\mathcal{E}(k_p)$ , computed with and without multiplication by

$$\frac{2\pi \bar{k}_p}{\Delta k_{\perp}} \cdot \frac{1}{C(p)}, \quad (28)$$

203 and averaged over 20 or 200 samples, is plotted as a function of  $k_p \Delta x$  in Fig. 2. As expected  
 204 for two-dimensional white noise, the energy spectral density increases roughly linearly with  
 205 wavenumber over the interval  $[0, \pi]$ . Whether averaged over 20 or 200 samples, the uncompen-  
 206 sated spectra (blue lines) look quite similar, and show significant noise. On the other hand, the  
 207 energy spectral densities compensated through multiplication by (28) look much smoother and the  
 208 remaining noise is greatly reduced as the sample size is increased from 20 to 200. Multiplication  
 209 by (28) also corrects these spectra for wavelengths shorter than  $2\Delta x$  (i.e., for wavenumbers in the  
 210 range  $\pi \leq k_p \Delta x \leq \sqrt{2}\pi$ ), but one should not attach confidence to results for such wavelengths in  
 211 practice.

212 Figure 3 shows the mean horizontal KE spectral density in a 20-member ensemble of numerical  
 213 simulations of idealized squall lines, initialized with slightly different humidity fields, conducted  
 214 using a  $512 \times 512$  periodic domain. In addition to the ensemble average, the spectra were averaged  
 215 over the vertical layer  $10 \leq z \leq 12$  km (Weyn and Durran 2017, Fig. 6e). The blue curve shows the  
 216 spectra computed using Python’s `numpy.fft` and (25); the red curve shows the same result, shifted  
 217 down by a factor of 10 for visibility, after compensating for the discretization noise by multiplying  
 218 by the factor (28), in which case the compensated KE spectral density is

$$\check{E}_c(k_p) = \frac{L^2 \bar{k}_p}{4\pi N^4 C(p)} \sum_{l,m \in R(p)} (\hat{u}_{l,m} \hat{u}_{l,m}^* + \hat{v}_{l,m} \hat{v}_{l,m}^*). \quad (29)$$

219 Despite the vertical and ensemble averaging, the uncompensated KE spectrum remains noisy. The  
 220 compensated KE spectrum, on the other hand, is quite smooth.

## 221 5. Relationship between one- and two-dimensional power-law spectra

222 If the two-dimensional KE spectral density of a non-divergent isotropic flow obeys the power-  
 223 law  $E(k_h) = \alpha_2 k_h^\beta$ , for  $\beta < 0$ , one-dimensional KE spectral densities obey the same power law,

224 with a different constant of proportionality, i.e.,  $E_1(k_x) = \alpha_1 k_x^\beta$ . Most atmospheric observations  
 225 are analyzed along lines (for example, along an aircraft flight track). If one wishes to compare two-  
 226 dimensional KE spectra from a model with observations of one-dimensional spectra, one should  
 227 correct for the difference between  $\alpha_1$  and  $\alpha_2$ . Leith (1971) showed that

$$E_1(k_x) = \frac{2}{\pi} \int_{k_x}^{\infty} \frac{E(k_h)}{(k_h^2 - k_x^2)^{1/2}} dk_h, \quad (30)$$

228 or letting  $s = k_h/k_x$ ,  $ds = dk_h/k_x$  and substituting for  $E(k_h)$ ,

$$E_1(k_x) = \frac{2\alpha_2 k_x^\beta}{\pi} \int_1^{\infty} \frac{s^\beta}{(s^2 - 1)^{1/2}} ds. \quad (31)$$

229 Leith (1971) noted that for  $\beta = -3$ ,  $\alpha_1 = \alpha_2/2$ , but did not consider other values of  $\beta$ . For  $\beta < 0$   
 230 the integral in (31) converges, giving

$$E_1(k_x) = \frac{\Gamma(-\frac{\beta}{2})}{\sqrt{\pi}\Gamma(\frac{1}{2} - \frac{\beta}{2})} E(k_x). \quad (32)$$

231 If  $\beta = -1$ ,  $\alpha_1 = \alpha_2$ , and in the important case  $\beta = -5/3$ ,  $\alpha_1 \approx 0.713\alpha_2$  (Lindborg 1999; Durran  
 232 and Gingrich 2014).

233 The analytic result (32) does not exactly hold for spectra computed from gridded data due to  
 234 numerical errors. To assess the nature of these errors, nondivergent flows were computed from a  
 235 streamfunction of the form

$$\hat{\psi}(k_x, k_y) = e^{i\phi} (k_x^2 + k_y^2)^{(\beta-3)/2}$$

236 where  $(k_x, k_y)$  are the wavenumber pairs for the discrete data,  $\phi \in [-\pi, \pi]$  is a random phase, and  
 237 the condition  $\hat{\psi}(k_x, k_y) = \hat{\psi}^*(-k_x, -k_y)$  is enforced to ensure  $\psi(x, y)$  is real. According to (15),  
 238 the horizontal velocities

$$\hat{u} = -ik_y \hat{\psi}, \quad \hat{v} = ik_x \hat{\psi},$$

239 will yield a KE spectral density for which  $E(k_h) \propto k_h^\beta$ .

240 One- and two-dimensional KE spectral densities, computed from single realizations of this ide-  
 241 alized velocity field on a  $512 \times 512$  isotropic mesh, are plotted in Fig. 4 for the cases  $\beta = -3$ ,  
 242  $-5/3$  and  $-1$ . The 1D spectral densities were computed from (13) using one-dimensional trans-  
 243 forms along the  $x$ -coordinate at each of the 512  $y$ -coordinate values, and then averaged over  $y$ . The  
 244 2D spectral densities were computed from (29) and scaled by the factor  $\alpha_1(\beta)/\alpha_2(\beta)$ .

245 As evident in Fig. 4, the  $\alpha_1/\alpha_2$  scaling does a good job of mapping the 2D spectra exactly onto  
 246 the corresponding 1D curve. Nevertheless, the 2D spectra fall slightly below the 1D spectra and  
 247 the expected  $k_p^\beta$  line at very small wavenumbers. This is due to the previously discussed issue of  
 248 coarse numerical resolution at very small wavenumbers. In contrast, at very large wavenumbers,  
 249 it is the 1D spectra that fall below the  $k_p^\beta$  line, and the discrepancy becomes much larger as  $\beta$   
 250 increases from  $-3$  to  $-1$ . This difference arises because, instead of extending to infinity, the nu-  
 251 merical equivalent of the integral (30) is effectively truncated at  $k_x = k_{\max} = \pi/\Delta x$ . When  $\beta = -3$ ,  
 252 the contribution from the unresolved high wavenumbers, and the high-wavenumber difference be-  
 253 tween the 1D and 2D spectra is much smaller than when  $\beta = -1$ . Although the high-wavenumber  
 254 fall-off in the amplitude of the 1D spectra in Fig. 4 is much weaker than that caused by numerical  
 255 dissipation in typical numerical simulations (as illustrated for example in Fig. 3), it is worth noting  
 256 that a modest fall-off should be expected at high wavenumbers even in the absence of dissipation.

257 The derivation of (32) assumes non-divergent two-dimensional isotropic flow, but the relation-  
 258 ship between  $\alpha_1$  and  $\alpha_2$  can also hold in at least some completely divergent, anisotropic flows.  
 259 This good behavior is illustrated in Fig. 5, which compares 1D and 2D spectra from the ensemble  
 260 of squall-line simulations already considered in Fig. 3. The total flow is decomposed into diver-  
 261 gent and rotational components as described in Weyn and Durran (2017), who also noted that the  
 262 divergent component closely follows a  $k_h^{-5/3}$  spectrum. Scaling the 2D divergent KE spectrum  
 263 such that  $\alpha_1 = 0.713\alpha_2$  maps the 1D and 2D spectra onto almost the same curve. In contrast, the

264 rotational KE does not follow a power-law as closely (i.e., it does not plot as a straight line), and  
265 the slopes of the 1D and 2D spectra are not as similar as those for the divergent winds.

## 266 6. Conclusions

267 In this paper we have considered the computation of horizontal KE spectra as our primary ex-  
268 ample, but equivalent expressions apply when computing the spectrum of any scalar variable.  
269 The correct dimensional scaling of the energy density spectra depends strongly on the normal-  
270 ization used in the discrete Fourier transform routines. The “traditional” choice of  $n_1 = 1/N$ ,  
271  $n_2 = 1$  in (1) and (2) leads to the relatively intuitive expressions (9) and (20) for the one- and two-  
272 dimensional KE spectral density, respectively. Matlab and Python’s `numpy.fft` routines use the  
273 alternative normalization  $(n_1, n_2) = (1, 1/N)$  and as a consequence, the corresponding KE spectral  
274 densities (13) and (24) differ for those computed with the traditional choice by factors of  $N^2$  in the  
275 one-dimensional case and  $N^4$  in a square two-dimensional domain.

276 Two-dimensional spectra computed by summing over wavenumber pairs  $(k_x, k_y)$  in annular bins  
277 exhibit systematic noise owing to the non-smooth increase in the count of wavenumber pairs in  
278 each bin as the total wavenumber  $k_h$  increases. One can compensate for this noise by multiplying  
279 the energy spectral density at each discrete  $k_h$  by the factor (28). If the underlying data are suffi-  
280 ciently smoothed by ensemble, temporal, or spatial averaging, the improvement produced by this  
281 procedure can be pronounced.

282 If the two-dimensional KE spectral density is proportional to  $k_h^\beta$  and  $\beta < 0$ , one-dimensional  
283 spectral densities for the same flow will follow the same  $k_h^\beta$  power law, but with a different con-  
284 stant of proportionality given by (32). This theoretical result is formally derived for isotropic  
285 nondivergent flows, but was found to also work well for a divergent anisotropic example. In the  
286 discrete case, the truncation of the data at some maximum wavenumber leads to a modest decrease



287 in the one-dimensional spectral density relative to the corresponding two-dimensional value at high  
 288 wavenumbers. Nevertheless, when  $\beta = -5/3$  the fall-off at high wavenumbers is much weaker  
 289 than that produced by numerical dissipation in typical atmospheric models.

290 *Acknowledgments.* The paper was improved through very helpful discussions with Mike Waite  
 291 and Jim Riley, and also by the comments of two anonymous reviewers. This research is funded by  
 292 NSF Grant AGS-1545927 and Grant N000141410287 from the Office of Naval Research (ONR).  
 293 JAW was supported by a National Defense Science and Engineering Graduate (NDSEG) Fellow-  
 294 ship.

## 295 APPENDIX

### 296 The discrete Parseval relation

297 A typical derivation of the discrete Parseval theorem is provided here to help the reader appreciate  
 298 the impact of different choices for  $n_1$  and  $n_2$ . From (2) and our previously defined notation,

$$u_j = n_2 \sum_{m=1}^N \hat{u}_m e^{2\pi i(m-1)(j-1)/N}. \quad (\text{A1})$$

299 Allowing for complex values of  $u_j$ , which is the most general case (and required as part of two-  
 300 dimensional Fourier transforms),

$$\begin{aligned} |u_j|^2 = |u_j u_j^*| &= n_2^2 \left( \sum_{m=1}^N \hat{u}_m e^{2\pi i(m-1)(j-1)/N} \right) \left( \sum_{m'=1}^N \hat{u}_{m'}^* e^{-2\pi i(m'-1)(j-1)/N} \right) \\ &= n_2^2 \sum_{m=1}^N \hat{u}_m \left( \sum_{m'=1}^N \hat{u}_{m'}^* e^{2\pi i(m-m')(j-1)/N} \right) \end{aligned}$$

301 Thus,

$$\sum_{j=1}^N |u_j|^2 = n_2^2 \sum_{m=1}^N \sum_{m'=1}^N \hat{u}_m \hat{u}_{m'}^* \sum_{j=1}^N \left( e^{2\pi i(m-m')/N} \right)^{(j-1)} \quad (\text{A2})$$

302 Using the finite sum of a geometric series

$$1 + q + q^2 + \dots + q^N = \frac{1 - q^{N+1}}{1 - q},$$

303 for  $m \neq m'$  the last summation in (A2) becomes

$$\sum_{j=1}^N \left( e^{2\pi i(m-m')/N} \right)^{(j-1)} = \frac{1 - e^{2\pi i(m-m')/N}}{1 - e^{2\pi i(m-m')/N}} = 0.$$

304 If  $m = m'$ , the last summation in (A2) is simply  $N$ , and therefore (A2) reduces to

$$\sum_{j=1}^N |u_j|^2 = N n_2^2 \sum_{m=1}^N \hat{u}_m \hat{u}_m^*, \quad (\text{A3})$$

305 showing that the choice  $n_2 = 1$  yields (5), whereas  $n_2 = 1/N$  gives (10).

## 306 **References**

- 307 Bartello, P., 1995: Geostrophic adjustment and inverse cascades in rotating stratified turbulence.  
308 *J. Atmos. Sci.*, **52**, 4410–4428.
- 309 Cho, J. Y. N., and Coauthors, 1999: Horizontal wavenumber spectra of winds, temperature, and  
310 trace gases during the Pacific Exploratory Missions: 1. Climatology. *J. Geophys. Res.*, **104 (D5)**,  
311 5697–5716, doi:10.1029/98JD01825.
- 312 Cooley, J., P. Lewis, and P. Welch, 1970: The fast Fourier transform algorithm: Programming  
313 considerations in the calculation of sine, cosine and Laplace transforms. *J. Sound Vib.*, **12**, 315–  
314 337.
- 315 Denis, B., J. Coté, and R. Laprise, 2002: Spectral decomposition of two-dimensional atmospheric  
316 fields on limited-area domains using the discrete cosine transform (DCT). *Mon. Wea. Rev.*, **130**,  
317 1812–1829.
- 318 Durran, D. R., 2010: *Numerical Methods for Fluid Dynamics: With Applications to Geophysics*.  
319 2nd ed., Springer-Verlag, New York, 516 p.
- 320 Durran, D. R., and M. Gingrich, 2014: Atmospheric predictability: Why butterflies are not impor-  
321 tant. *J. Atmos. Sci.*, **71**, 2476–2488.

322 Durran, D. R., and J. Weyn, 2016: Thunderstorms do not get butterflies. *Bull. Amer. Meteor. Soc.*,  
323 **97**, 237–243.

324 Errico, R., 1985: Spectra computed from a limited area grid. *Mon. Wea. Rev.*, **113**, 1554–1562.

325 Hamilton, K., Y. O. Takahashi, and W. Ohfuchi, 2008: Mesoscale spectrum of atmospheric mo-  
326 tions investigated in a very fine resolution global general circulation model. *J. Geophys. Res.*,  
327 **113**, D18 110.

328 Leith, C., 1971: Atmospheric predictability and two-dimensional turbulence. *J Atmos Sci*, **28**,  
329 145–161.

330 Lindborg, E., 1999: Can the atmospheric kinetic energy spectrum be explained by two-  
331 dimensional turbulence? *J. Fluid Mech.*, **388**, 259–288.

332 Nastrom, G., and K. Gage, 1985: A climatology of atmospheric wavenumber spectra of wind and  
333 temperature observed by commercial aircraft. *J. Atmos. Sci.*, **42**, 950–960.

334 Salvador, R., J. Calbó, and M. M. Millán, 1999: Horizontal grid size selection and its influence on  
335 mesoscale model simulations. *J. Appl. Meteor.*, **38**, 1311–1329.

336 Skamarock, W. C., 2004: Evaluating mesoscale NWP models using kinetic energy spectra. *Mon.*  
337 *Wea. Rev.*, **132**, 3019–3024.

338 Tanguay, M., P. Bartello, and P. Gauthier, 1995: Four-dimensional data assimilation with a wide  
339 range of scales. *Tellus A*, **47**, 974–997.

340 Tennekes, H., and J. Lumley, 1972: *A First Course in Turbulence*. MIT Press, Cambridge, 300 p.

341 Waite, M. L., 2016: Dependence of model energy spectra on vertical resolution. *Mon. Wea. Rev.*,  
342 **144**, 1407–1421.

343 Weyn, J. A., and D. R. Durran, 2017: The dependence of the predictability of mesoscale convective  
344 systems on the horizontal scale and amplitude of initial errors in idealized simulations. *J. Atmos.*  
345 *Sci.*, **74**, 2191–2210.

346  
347  
348  
349  
350  
  
351  
352  
353  
354  
355  
  
356  
357  
358  
359  
360  
  
361  
362  
363  
364  
365  
  
366  
367  
368  
369  
370

**LIST OF FIGURES**

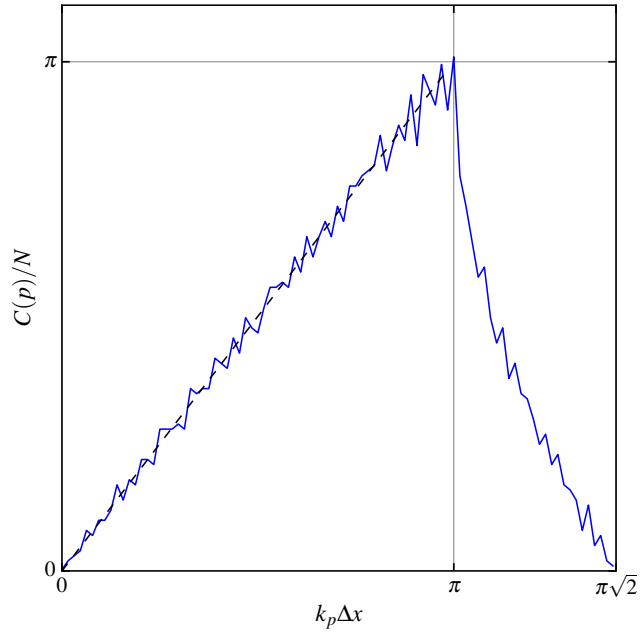
**Fig. 1.** Normalized number of wavenumber pairs within each total wavenumber bin  $C(p)/N$  plotted as a function of  $k_p\Delta x$ , for a square domain with 128 grid points along each coordinate (blue). The black dashed line shows the expected number of wavenumber pairs for each  $k_p\Delta x$  over the interval  $0 \leq k_p\Delta x \leq \pi$ . . . . . 22

**Fig. 2.** Two-dimensional energy spectral density for random white noise in a  $128 \times 128$  square domain averaged over (a) 20 samples, (b) 200 samples. The blue line is the result of the standard summation over annular rings in the wavenumber domain; the red line shows the result after multiplication by the noise compensating factor (28), shifted down by a factor of 10 for clarity. The top axis is labeled in units of wavelength divided by  $\Delta x$ . . . . . 23

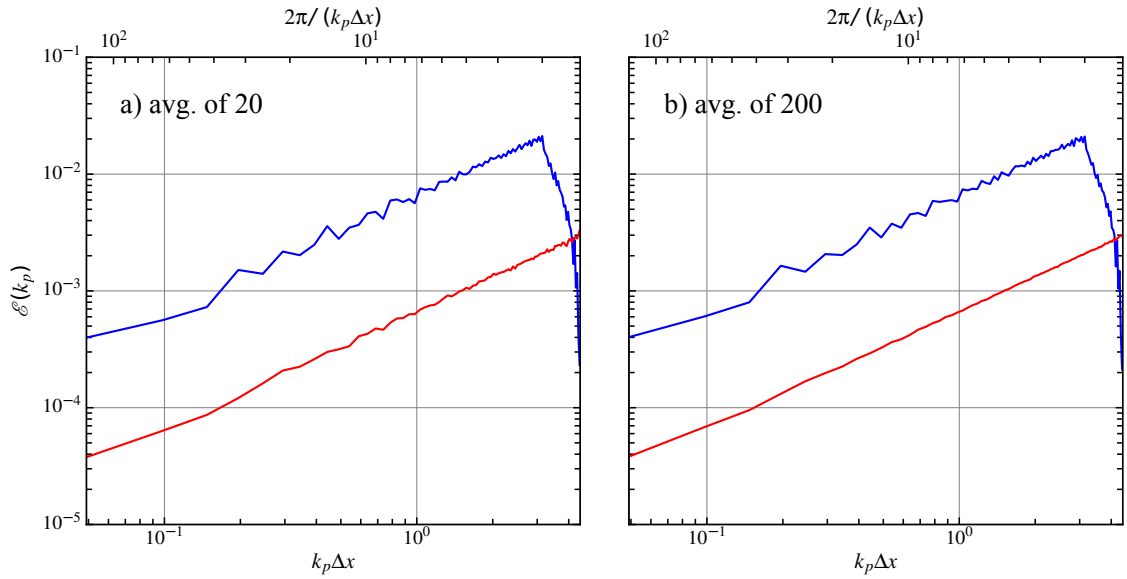
**Fig. 3.** Two-dimensional KE spectral density from idealized squall-line simulations. The blue line is the result of the standard summation over annular rings in the wavenumber domain. The red line shows the result after multiplication by the noise-compensating factor (28) and is shifted down by a factor of 10 for better visibility. The portion of the spectrum corresponding to wavelengths shorter than  $7\Delta x$  is shaded. The thick gray line follows a  $k^{-5/3}$  slope. . . . . 24

**Fig. 4.** One-dimensional (dashed) and two-dimensional (dotted) KE spectral densities plotted as a function of  $k_x\Delta x$  and  $k_p\Delta x$ , respectively for nondivergent velocity fields analytically specified on an isotropic  $512 \times 512$  mesh to follow  $k_h^{-3}$  (red),  $k_h^{-5/3}$  (blue), and  $k_h^{-1}$  (green) spectral slopes. The blue lines are shifted up by a factor of 10 for better visibility. The top axis is labeled in units of wavelength divided by  $\Delta x$ . . . . . 25

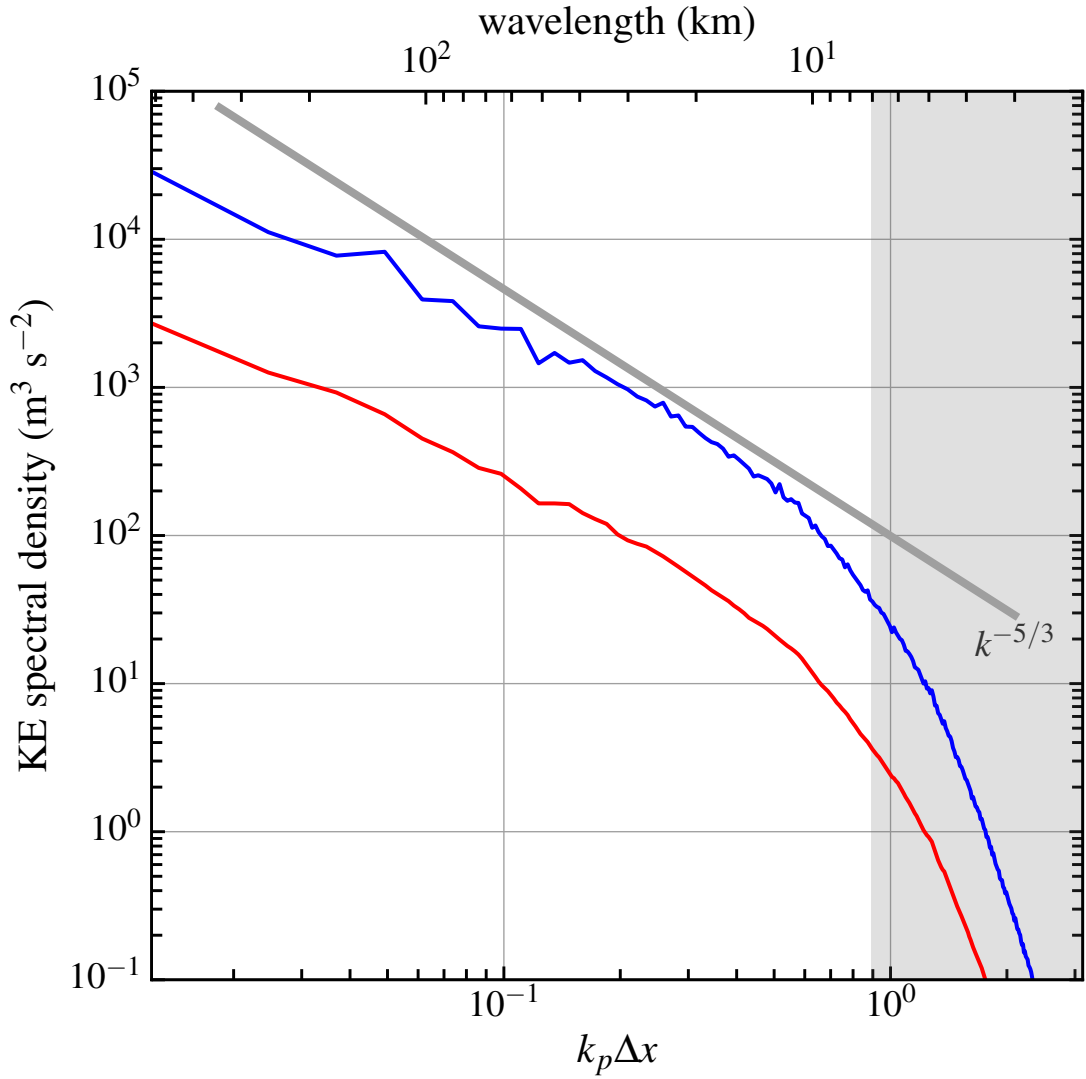
**Fig. 5.** One-dimensional (dashed) and two-dimensional (dotted) KE spectral densities plotted as a function of  $k_x\Delta x$  and  $k_p\Delta x$ , respectively for the ensemble of squall-line simulations shown in Fig. 3. Black curves are the full KE; blue curves are the KE of the divergent component, reduced by a factor of 10 for visibility; red curves are the KE of the rotational component, reduced by a second factor of 10. The top axis is wavelength in units of  $\Delta x$ . . . . . 26



371 FIG. 1. Normalized number of wavenumber pairs within each total wavenumber bin  $C(p)/N$  plotted as a  
 372 function of  $k_p \Delta x$ , for a square domain with 128 grid points along each coordinate (blue). The black dashed line  
 373 shows the expected number of wavenumber pairs for each  $k_p \Delta x$  over the interval  $0 \leq k_p \Delta x \leq \pi$ .

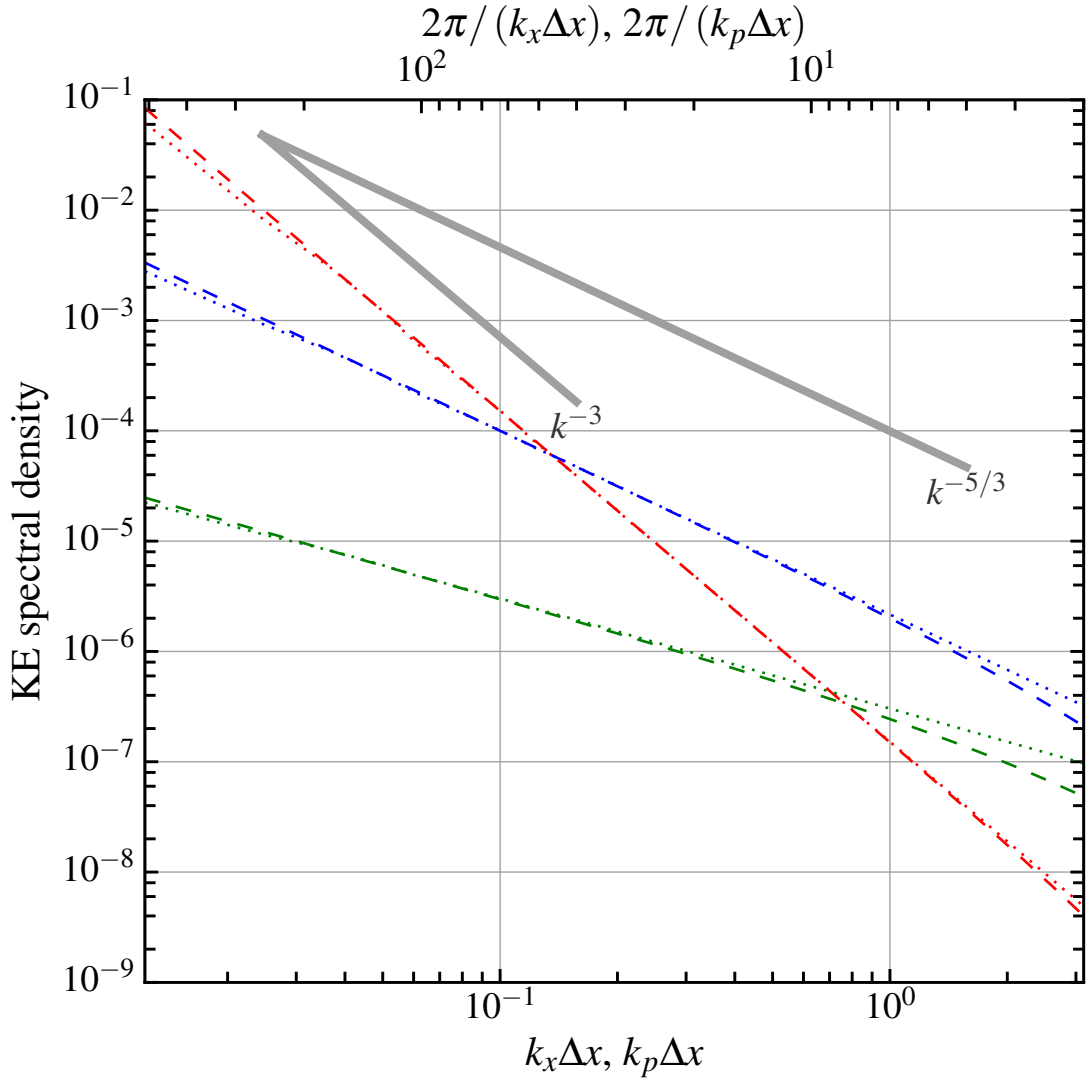


374 FIG. 2. Two-dimensional energy spectral density for random white noise in a  $128 \times 128$  square domain aver-  
 375 aged over (a) 20 samples, (b) 200 samples. The blue line is the result of the standard summation over annular  
 376 rings in the wavenumber domain; the red line shows the result after multiplication by the noise compensating  
 377 factor (28), shifted down by a factor of 10 for clarity. The top axis is labeled in units of wavelength divided by  
 378  $\Delta x$ .

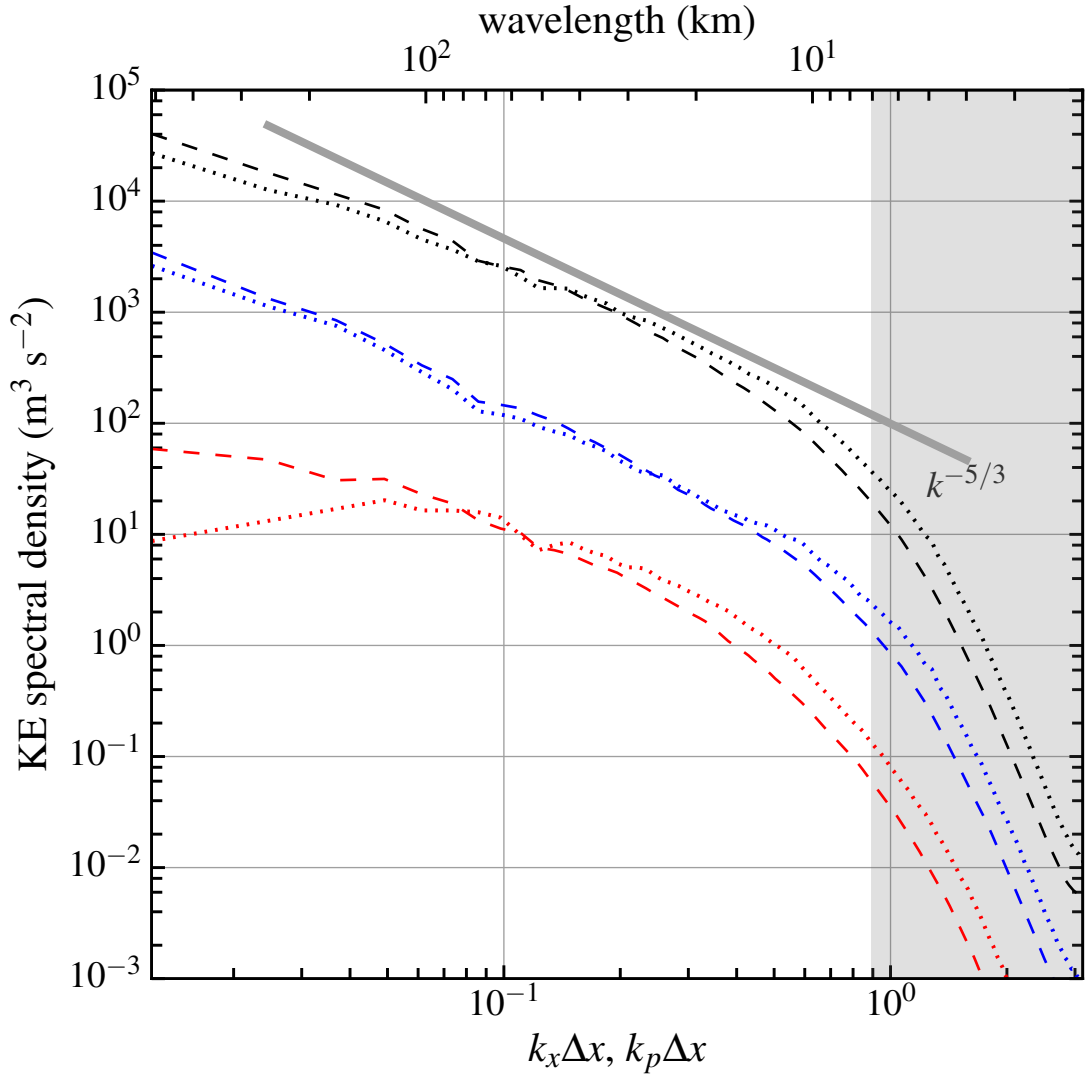


379 FIG. 3. Two-dimensional KE spectral density from idealized squall-line simulations. The blue line is the result  
 380 of the standard summation over annular rings in the wavenumber domain. The red line shows the result after  
 381 multiplication by the noise-compensating factor (28) and is shifted down by a factor of 10 for better visibility.  
 382 The portion of the spectrum corresponding to wavelengths shorter than  $7\Delta x$  is shaded. The thick gray line  
 383 follows a  $k^{-5/3}$  slope.





384 FIG. 4. One-dimensional (dashed) and two-dimensional (dotted) KE spectral densities plotted as a function  
 385 of  $k_x \Delta x$  and  $k_p \Delta x$ , respectively for nondivergent velocity fields analytically specified on an isotropic  $512 \times 512$   
 386 mesh to follow  $k_h^{-3}$  (red),  $k_h^{-5/3}$  (blue), and  $k_h^{-1}$  (green) spectral slopes. The blue lines are shifted up by a factor  
 387 of 10 for better visibility. The top axis is labeled in units of wavelength divided by  $\Delta x$ .



388 FIG. 5. One-dimensional (dashed) and two-dimensional (dotted) KE spectral densities plotted as a function  
 389 of  $k_x \Delta x$  and  $k_p \Delta x$ , respectively for the ensemble of squall-line simulations shown in Fig. 3. Black curves are the  
 390 full KE; blue curves are the KE of the divergent component, reduced by a factor of 10 for visibility; red curves  
 391 are the KE of the rotational component, reduced by a second factor of 10. The top axis is wavelength in units of  
 392  $\Delta x$ .